

# Thermal and Mechanical Stabilities of Core-shell Microparticles Containing a Liquid Core

Fariba Malekpour Galogahi

Griffith University

Hongjie An

Griffith University

Yong Zhu

Griffith University <https://orcid.org/0000-0001-6701-5694>

Nam-Trung Nguyen (✉ [nam-trung.nguyen@griffith.edu.au](mailto:nam-trung.nguyen@griffith.edu.au))

Griffith University <https://orcid.org/0000-0003-3626-5361>

---

## Research Article

**Keywords:** core-shell particle, liquid core, thermal stability, mechanical stability, microfluidics

**Posted Date:** September 15th, 2021

**DOI:** <https://doi.org/10.21203/rs.3.rs-870641/v2>

**License:** © ⓘ This work is licensed under a Creative Commons Attribution 4.0 International License.

[Read Full License](#)

---

**Version of Record:** A version of this preprint was published at Journal of Molecular Liquids on December 1st, 2021. See the published version at <https://doi.org/10.1016/j.molliq.2021.117726>.

1 **Thermal and Mechanical Stabilities of Core-shell Microparticles Containing a Liquid**  
2 **Core**

3  
4 *Fariba Malekpour Galogahi, Hongjie An, Yong Zhu, Nam-Trung Nguyen\**

5  
6  
7 Queensland Micro- and Nanotechnology Centre, Griffith University, 170 Kessels Road,  
8 Nathan, 4111 Queensland, Australia  
9 E-mail: nam-trung.nguyen@griffith.edu.au

10  
11 **Abstract**

12 Thorough understanding of the behaviour of core-shell microparticles with a liquid core is  
13 essential for determining their performance in applications under different operation conditions.  
14 This paper reports the behaviour of core-shell particles with a liquid core under thermal and  
15 mechanical loads. First, we formulated an analytical model for the heating process of a core-  
16 shell microparticle with a liquid core. Next, we utilised an axisymmetric model of an elastic  
17 spherical shell upon compression to describe the deformation of a core-shell microparticle.  
18 Finally, we conducted experiments to validate these models. Both thermal and mechanical  
19 models agree well with the experimental data. The maximum temperature a core-shell  
20 microparticle can withstand depends on the liquid, the geometry, and the material of the shell.  
21 The critical compression force before rupture of a core-shell microparticle depends on the  
22 Poisson's ratio of the shell material and the shell thickness relative to the outer shell radius. The  
23 rupture force and rupture temperature increase with increasing shell thickness.

24 Keywords: core-shell particle, liquid core, thermal stability, mechanical stability, microfluidics  
25

26 **1. Introduction**

27 Recently, core-shell microparticles have attracted increasing attention from the research  
28 community due to the relatively simple manipulation, versatile choice of materials, and  
29 modifiable surface properties, as well as their broad range of applications in biomedicine,  
30 biotechnology, and chemistry [1]. For instance, encapsulation is a promising technique for  
31 modern laundry powders, which allow the co-existence of enzyme and surfactants, enabling

32 fragrance molecules to stay with clothes during and after washing, and keep bleaches stable and  
33 effective. Microcapsules packed with a small amount of liquid core are used as micro-reactors,  
34 storage containers, and delivery carrier for food, drug, coating, and cosmetic products [2]. These  
35 microcapsules are usually formed by single emulsion or double emulsion techniques such as  
36 magnetic stirring [3], vortex mixing [4] electro-spraying [5], and microfluidics. Digital  
37 microfluidics is remarkably efficient compared to other techniques in terms of producing stable  
38 and monodispersed core-shell microcapsules. The formation process of double emulsion can be  
39 controlled on chip with integrated control system [6], temperature sensing and control [7, 8],  
40 and enhanced heat ad mass transfer [9]. Furthermore, many applications require the controlled  
41 release of the liquid core from the microcapsules [2]. Some microcapsules for drug delivery or  
42 implant are designed to be permeable and liquid core can be released continuously [10].  
43 However, a porous shell could be a problem for storage, limiting its use for encapsulating small  
44 molecules [11]. Other core-shell microcapsules are designed to be impermeable and only  
45 release their contents by rupture, such as mechanical friction or compression [12], pH change  
46 [13], enzymatic degradation, and thermal stress [14, 15].

47 Understanding the mechanical and thermal properties of core-shell microparticles is crucial for  
48 their design, synthesis, handling, and application. First, thermal properties of both core and  
49 shell materials determine the operation temperature for applications such as storage, cargo  
50 delivery, sensing, and cell culture [16]. Thermal curing of the shell can be problematic for a  
51 volatile liquid core or solvent with low boiling temperature [14]. Packing an organic core in an  
52 inorganic shell can improve its thermal stability [17]. Generally, previous studies suggest three  
53 possible mechanisms that control the thermally induced release of core contents from  
54 microcapsules: (i) the burst of the shell due to the high thermal expansion coefficient of liquid  
55 core and subsequently increased internal thermal stresses [18, 19]; (ii) the permeation and  
56 diffusion of the core contents through the porous or permeable microcapsule shell; and (iii) the

57 degradation of microcapsule shell at the high temperature [19]. The release mechanism is an  
58 essential factor for later applications, for which, e.g., the thermal stability of shell as a thermal  
59 protection layer is important or controlled release of core components at a specific temperature  
60 is desirable. The thermal stability is correlated with thermal tolerance of microcapsules in the  
61 actual applications such as the temperature of storage and delivery of cargo, triggering  
62 temperature in catalysis, and thermal tolerance of sensing systems [20]. Furthermore, size and  
63 thickness of the shell affect the thermal behaviour of core-shell microparticles. The rupture  
64 temperature has been found increase exponentially with decreasing size of the microcapsules.  
65 A critical threshold size of approximately 10  $\mu\text{m}$  was reported by Zhao et al.[20]. However, the  
66 thermal behaviour of liquid core-shell microparticles is not yet fully understood due to the lack  
67 of a theoretical model.

68         Intrinsic mechanical properties of microcapsules, particularly of the shell, affect their  
69 performance. Under some circumstances, the release of encapsulated substances require stress,  
70 e.g. massage for the release of perfume for personal skin care, and compression for encapsulated  
71 ink in inkless paper and dyes in textile. The hydrodynamic shear stress in blood vessels is a  
72 major problem for microcapsules in drug delivery [21]. Core-shell capsules for scaffolds in  
73 tissue engineering, for instance in bone and cartilage, are expected to withstand a high  
74 mechanical stress [22]. A number of characterisation methods of mechanical properties of core-  
75 shell microparticles can be found in a recent review paper [23]. Compression of microcapsule  
76 of 10- $\mu\text{m}$  diameter were investigated by nanoindentation with an atomic force microscopy  
77 (AFM) with relatively high spatial resolution [24]. Capsules with diameters on the order of  
78 100  $\mu\text{m}$  are too big to be measured by AFM, and are usually characterised by compression  
79 between two parallel plates using a micromanipulator [24]. Among these characterisation  
80 methods, compression between two flat parallel plates is an effective mean to assess the rupture  
81 of the shell, as well as the elasticity of the microcapsule. Early compression studies indicated

82 that the deformation under compression largely depends on the shell material, and the rupture  
83 force increases with increasing size of the microparticles [25]. Compression of different liquid  
84 core-shell microcapsules were studied and tested [26-29] using the axisymmetric model of a  
85 thin-shell microcapsules compressed between two parallel flat plates. Bando et al. proposed the  
86 assumption of no initial stretch of the shell which caused numerical instability and developed a  
87 new model [30]. However, the model may lead to errors for thick-wall capsules, because the  
88 effect of bending stress cannot be neglected [31, 32].

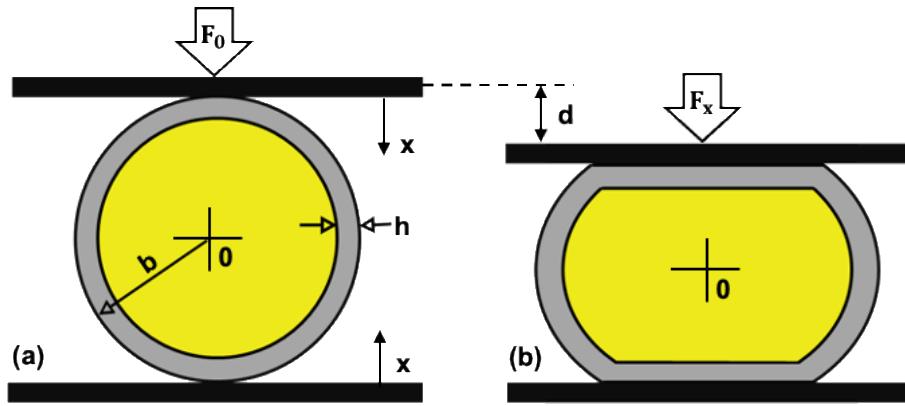
89 We previously prepared core-shell microparticles consisting of a HFE7500 fluorinated  
90 oil core and a polymer shell of trimethylolpropane trimethacrylate (TMPTMA) using droplet-  
91 based microfluidics [33, 34]. The core-shell microparticles can be tuned for different ratios of  
92 shell thickness to outer radius. However, little information is available on thermal and  
93 mechanical properties of these particles. The present study aims to experimentally investigate  
94 the behaviour of core-shell microparticles with a liquid core during heating and compression  
95 processes. The experimental results are compared with analytical models considering  
96 parameters such as particle size and shell thickness. The thermal model predicts the stress  
97 induced by the thermal expansion of the liquid core during the heating process acting on the  
98 shell layer. The axisymmetric model of an elastic spherical shell can describe the behaviour of  
99 the core-shell microparticle under compression.

## 100 **2. Analytical models**

### 101 **2.1. Mechanical behaviour of a core-shell particle with liquid core**

102 Next, we considered a thick-walled spherical shell of thickness  $h=b-a$  and the elastic modulus  
103  $E$  fully filled with a liquid, Fig. 1(a). For simplicity, the liquid was considered as  
104 incompressible, so the pressure was solely applied to the shell. The shell material was  
105 assumed to be homogeneous, impermeable, elastic, and isotropic. The thickness  $h$  was

106 assumed to remain constant without any bend or inflation during the compression process,  
 107 and the internal volume of the shell remains constant as it deforms. The shell is compressed  
 108 between two rigid horizontal plates, Fig. 1(b). Because of the compression, the shell deforms  
 109 symmetrically with a distance  $x$  from top and bottom each and a total displacement of  $d=2x$ .



110

111 **Figure 1.** Compression process of a thick-walled spherical core-shell particle: (a) Initial state;  
 112 (b) Deformed state.

113 We first used the Pauchard's model to find the elastic energy stored in the spherical  
 114 elastic shell. Pauchard and Rica [35] considered two different compression regimes: (i) the first  
 115 flattening cap of a spherical shell into a flat plane under low force and then (ii) axisymmetric  
 116 inwards buckling of the flattened portion of shell resulted from a higher load. In the first regime,  
 117 the spherical shell is flattened against the horizontal surfaces. The elastic energy of this regime  
 118 is:

$$119 \quad U_1 = A \frac{1}{4} \frac{Eh^{5/2}}{b} x^{3/2} + B \frac{Eh}{b} x^3, \quad (1)$$

120 where  $A$  and  $B$  are dimensionless constants depending on the properties of the shell material  
 121 through the Poisson's ratio  $\nu$ . We determined these constants experimentally through curve  
 122 fitting across all experiments using core-shell particles of the same shell material but different

123 geometries. The first term represents the energy that results from axisymmetric folding of the  
 124 spherical shell and balancing the bending and stretching energy of the flattened surface. The  
 125 second term accounts for the energy of compression and flattening out a part of the spherical  
 126 shell [35, 36]. The applied force  $F$  causing the displacement  $x$  from each side of the sphere can  
 127 then be obtained by differentiating the elastic energy (9):

$$128 \quad F_x = A \frac{3Eh^{5/2}}{8b} x^{1/2} + 3B \frac{Eh}{b} x^2 \quad (2)$$

129 The force  $F_x$  is expected to depend slightly on the Poisson's ratio  $\nu$ .

130 The elastic energy of buckling in the second regime is:

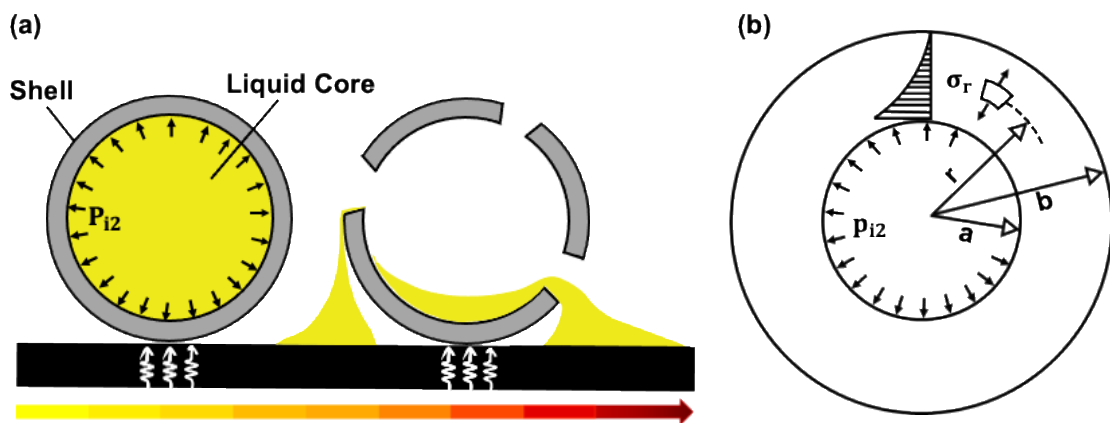
$$131 \quad U_2 = A \frac{Eh^{5/2}}{b} x^{3/2} + C \frac{Eh^3}{b} x \quad (3)$$

132 The total displacement reaches a critical value  $d_{\max} = 2x_{\max}$ , where the shell ruptures if  
 133 compression continues. The critical displacement can be determined by the continuity  
 134 condition  $U_1 = U_2$ . In the following section, we conducted experiments on liquid core-shell  
 135 particles generated by our microfluidic approach to determine the constants  $A$ ,  $B$  and  $C$  by fitting  
 136 the measured force versus displacement data.

## 137 **2.2. Thermal behaviour of a core-shell particle with liquid core**

138 In this section, the thermal characteristics of oil core-polymer shell particles are formulated  
 139 analytically. The core-shell particle is considered as a thick-walled particle because the wall  
 140 thickness is greater than a tenth of overall radius of the particle. Figure 2 shows the schematic  
 141 heating process of a core-shell particle and the forces acting on the spherical shell during the  
 142 heating process. Gradually increasing the temperature increases the pressure of the liquid and  
 143 induces a uniform pressure on the inner wall of the shell. Eventually, the pressure of the liquid

144 exceeds the maximum tensile strength of the shell and causes it to rupture, Figure 2(a). For  
 145 simplification and ease of presentation, the following assumptions were made for the model:  
 146 (i) The shell thickness of a core-shell particle remains constant and no curvature or slope occurs  
 147 during the heating process; (ii) The core is located at the centre of the particle; (iii) Both core  
 148 and shell are spherical and maintain this shape during the heating process; (iv) The volume of  
 149 the rigid shell remains unchanged during the heating process; (v) Temperature distribution is  
 150 uniform throughout the shell layer and the core; (vi) Pressure is uniformly distributed over the  
 151 inner wall of the shell and change gradually with temperature; (v) The liquid encapsulated  
 152 inside the shell is considered homogeneous and in a thermodynamic equilibrium states; and (vi)  
 153 The liquid core is assumed to be in a single-phase before the rupture of the shell.  
 154



155  
 156 **Figure 2.** (a) Schematic of the process through which a liquid core-shell particle undergoes  
 157 heat-induced change; (b) Model of a thick-walled spherical core-shell particle representing  
 158 internal pressure and induced stress [37].

159  
 160 For a single-phase oil core encapsulated in a solid shell, the volume  $V$ , the absolute temperature  
 161  $T$ , and pressure  $P$  are interdependent quantities. The relationships between  $V$ ,  $T$ , and  $P$  can be  
 162 generally described by an equation of state [38]:

163  $f(P, V, T) = 0$  (4)

164 This state equation allows for the expression of one quantity of volume, temperature, and  
 165 pressure in terms of the other two. For volume  $V(T, P)$  as a function of temperature and  
 166 pressure:

$$167 \quad dV = \left(\frac{\partial V}{\partial T}\right)_P dT + \left(\frac{\partial V}{\partial P}\right)_T dP, \quad (5)$$

168 considering a constant liquid volume  $dV = 0$ :

$$169 \quad 0 = \left(\frac{\partial V}{\partial T}\right)_P dT + \left(\frac{\partial V}{\partial P}\right)_T dP \quad (6)$$

170 and rearranging this equation for  $\partial P/\partial T$  results in:

$$171 \quad \left(\frac{\partial P}{\partial T}\right)_V = - \left(\frac{\partial V}{\partial T}\right)_P / \left(\frac{\partial V}{\partial P}\right)_T \quad (7)$$

172 In (4), the partial derivatives are related to the two thermodynamic coefficients, volume  
 173 expansion coefficient  $\alpha$ , and isothermal compressibility  $K$  with  $\alpha = \frac{1}{V} \left(\frac{\partial V}{\partial T}\right)_P$  and  $K = -\frac{1}{V} \left(\frac{\partial V}{\partial P}\right)_T$ ,  
 174 respectively. Substituting these coefficients into equation (7) results in:

$$175 \quad \left(\frac{\partial P}{\partial T}\right)_V = \frac{\alpha}{K} \quad (8)$$

176 Integrating both sides of (5) results in the final internal pressure  $P_{i2}$ :

$$177 \quad P_{i2} = P_{i1} + \frac{\alpha}{K} (T_2 - T_1), \quad (9)$$

178 where  $P_{i1}$  and  $T_1$  are the initial internal pressure and temperature, which are also the ambient  
 179 pressure and temperature,  $P_{i2}$  and  $T_2$  are the internal pressure and temperature of liquid core in  
 180 the final state. Considering temperature and pressure dependence, Dan et al. [39] proposed an  
 181 empirical isothermal compressibility model for HFE 7500 with an isothermal compressibility  
 182  $K$ :

$$183 \quad K = 0.07466 / \left[ \left( 1 - 0.07466 \ln \frac{\beta + P}{\beta + 0.1} \right) (\beta + P) \right] \quad (10)$$

184 with  $\beta = 308.2 - 1.301T + 1.414 \times 10^{-3}T^2$  and  $P$  are pressures in MPa.

185 Considering a spherical thick-walled shell shown in Figure 2(b), which is filled with the liquid  
186 and subjected to the pressure induced by heating, the spherically symmetrical solution leads  
187 to the normal stress inside the shell under the internal pressure  $P_{i2}$  [37]:

$$188 \quad \sigma_r = -\frac{a^3 P_{i2}}{r^3} \frac{b^3 - r^3}{b^3 - a^3} \quad (11)$$

189 Where  $a$  and  $b$  are the inner and outer radii of the shell, respectively.

### 190 **3. Experiment**

#### 191 **3.1. Materials**

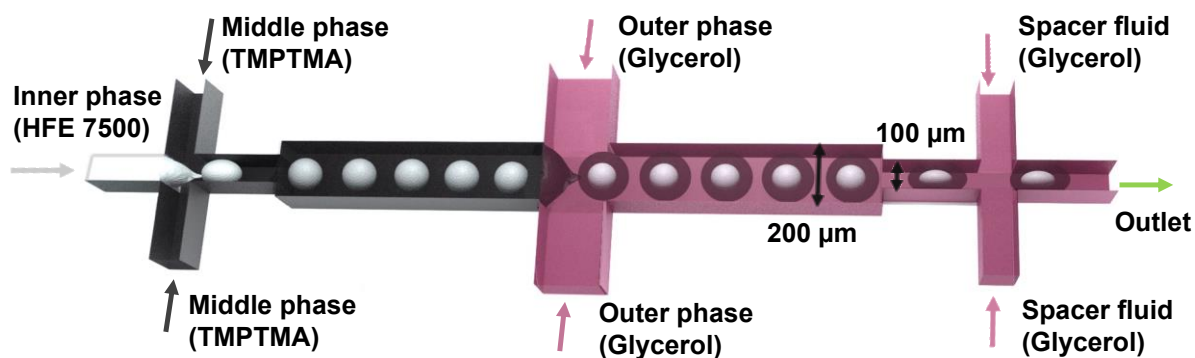
192 Fluorinated oil (HFE, Novec 7500 3M) was purchased from Sigma-Aldrich Chemical Reagent  
193 Co., Ltd. Ethyl- 4(dimethylamino)benzoate, camphorquinone, and trimethylolpropane  
194 trimethacrylate were purchased from Merck. All chemicals used in this study were of analytical  
195 grade and distilled water was used in all experiments.

#### 196 **3.2. Fabrication of microfluidic device**

197 The design of the microfluidic device used to produce core-shell droplets was previously  
198 reported [33]. We fabricated the PDMS microfluidic device using soft-lithography. The master  
199 mould with microfluidic channel patterns was fabricated in SU-8 on a silicon wafer by standard  
200 photolithography. Width and height of the microchannels are 200  $\mu\text{m}$  and 100  $\mu\text{m}$ , respectively.  
201 A mixture of PDMS and curing agent in a 10:1 ratio was poured into the mould master and then  
202 was degassed and cured at 75°C for 1 hour. The PDMS device was cut out from the mould. A  
203 biopsy punch with the same diameter as the tubing was used for punching the inlets and the  
204 outlets. The PDMS part was subsequently bonded onto glass after treating the bonding surfaces  
205 with air plasma. Finally, by passing water through the channels a hydrophilic PDMS device  
206 was obtained.

#### 207 **3.3. Preparation of core-shell particles**

208 The PDMS device has three cross junctions: HFE7500 oil was used as the inner phase at the  
209 first junction and to disperse HFE7500 oil and produce oil core; TMPTMA was used as the  
210 middle phase at this junction, Figure 3.



211

212 **Figure 3.** Schematic illustration of the flow focusing microfluidic device used for the  
213 generation of liquid core-shell microparticles.

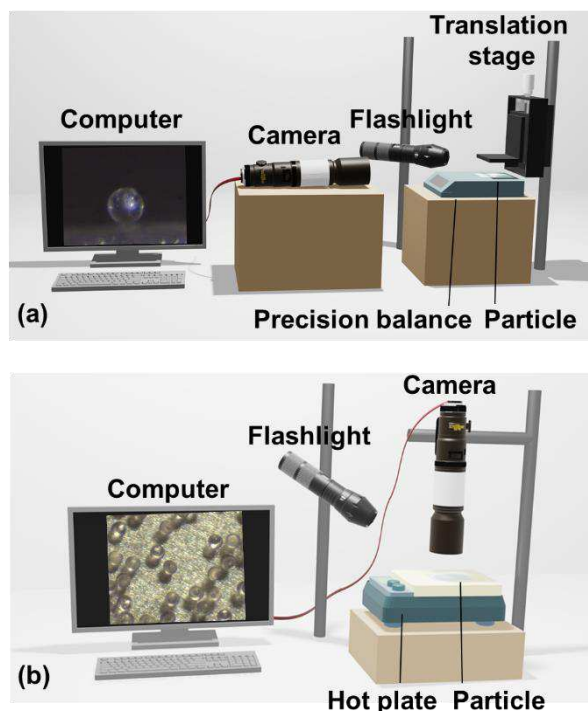
214 The TMPTMA was prepared by mixing ethyl- 4(dimethylamino)benzoate (0.06 g),  
215 camphorquinone (0.05 g), and TMPTMA (10 g) using mechanical stirred at 600 rpm for 1 hr  
216 [40]. Distilled water with glycerol (50% v/v) was used as the outer liquid phase at the second  
217 junction. The core-shell droplets generated were then transferred through the channel to the  
218 third junction and were collected at the outlet. The flow rates of all fluids were controlled using  
219 syringe pumps. The flow rate of TMPTMA was kept constant at 150 μL/hr. The flow rates of  
220 HFE7500 oil were set at 60, 100 and 140 μL/hr at the first junction to achieve core-shell  
221 particles with shell to outer radius ratios of 0.41, 0.33 and 0.21, respectively. The flow rates  
222 of glycerol were fixed at 800 and 3,000 μL/hr at the second and third junctions, respectively.  
223 The formation of core-shell droplets in the PDMS device was monitored using an inverted  
224 microscope (Nikon, Eclipse Ti) connected to a computer.

225 At the outlet, a long tubing was used to collect the generated core-shell droplets. Since  
226 the core-shell droplets tended to aggregate while passing through the outlet tubing, the tubing  
227 was exposed to an UV light to instantaneously cross-link the shell layer. However, the particles

228 did not completely polymerise due to the limited residence time. Hence, the collected particles  
229 were subsequently further exposed to UV light again for five minutes. The collected core-shell  
230 particles at the outlet were then washed once with methanol to dissolve the bulk polymer waste  
231 and to prevent particles from sticking during storage and drying. Finally, the generated core-  
232 shell microparticles were dried in a vacuum desiccator for 30 minutes. Optical microscopy  
233 images of the dried core-shell microparticles were then taken with a microscope (Eclipse Ti,  
234 Nikon).

### 235 **3.4. Mechanical behaviour of core-shell microparticles**

236 We characterised the mechanical properties of core-shell microparticles using compression  
237 between two parallel plates. Figure 4(a) shows a right-angle mounting adapter set up on a  
238 single-axis translation stage with a standard micrometre positioner was placed perpendicular to  
239 the pan of an analytical balance. A single core-shell particle on a microscope slide was placed  
240 on the balance pan. During the experiment, the side view of the particle was observed and  
241 recorded with a camera. The mounting adapter moved downward and compressed the core-  
242 shell microparticles. The applied load on the particles was measured using the precision  
243 balance. During the compression test, the force acting on the particle and the displacement  
244 corresponding to the deformation was recorded. Measurements were carried out for particles  
245 with different sizes. An inverted microscope (Nikon, Eclipse Ti) was used to determine the  
246 morphology and geometry of the dried core-shell microparticles were before each experiment.



247

248 **Figure 4.** Schematic of the experimental setups for investigations for: (a) the thermal behaviour  
 249 and (b) mechanical behaviour of core-shell microparticles with liquid core.

250

### 251 3.5. Thermal behaviour of core-shell microparticles

252 We carried out thermal stability experiments with a controlled hot plate, Figure 4(b). The  
 253 sample was placed on a glass slide, which was then placed on the hot plate. The measurements  
 254 were performed under atmospheric pressure with 5°C temperature increment from room  
 255 temperature until a change in the core-shell particles surface was observed. For an accurate  
 256 measurement, the core-shell particles were kept for 10 minutes at each temperature value. The  
 257 first scan was carried out from room temperature to the critical rupture temperature, when the  
 258 shell ruptures and the core liquid escapes. Three particle samples from different preparation  
 259 batches were studied and the average value was recorded. The different stages of heating were  
 260 recorded with a camera (Ximea xiQ-USB3 MQ013CG-ON) and a high-resolution  
 261 magnification lens (Edmund Optics) placed on top of the sample.

262

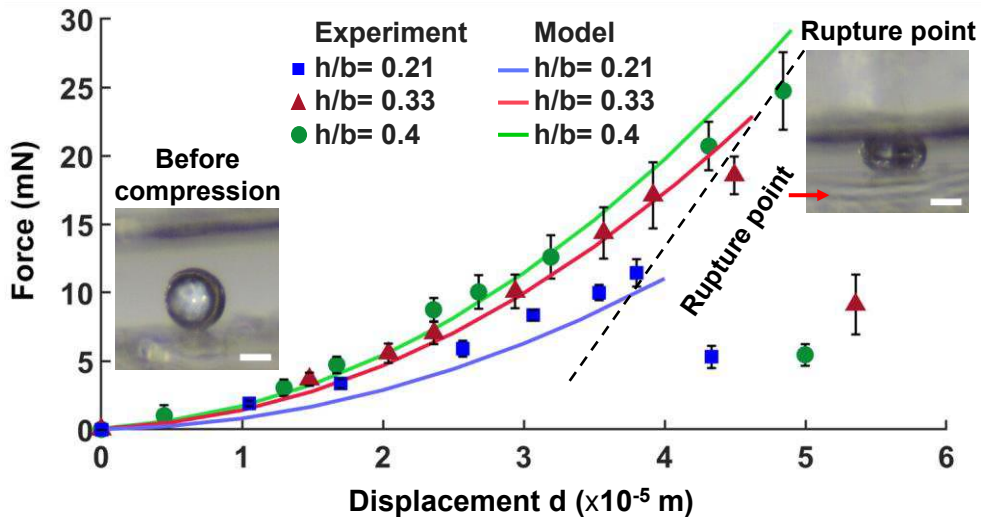
### 263 3.6. X-Ray Computed Microtomography (XCMT)

264 High resolution X-ray computed microtomography was also used to analyse 3D microstructure  
265 of core-shell microparticles. Dried core-shell particles were placed on a cylindrical holder that  
266 was covered with a clear tape. The holder was then placed on a precision rotating stage inside  
267 the chamber of an X-ray computed microtomography system (VersaXRM-500 High-Resolution  
268 3D X-ray Tomography Microscope System, ZEISS® Xradia, Pleasanton, CA, USA). The  
269 distance between the samples and the detector was fixed at 20 mm. In the measurements, the  
270 X-ray tube power and voltage were 3 W and 40 kV, respectively, with an exposure time of 20 s.  
271 X-ray images with a field of view (FOV) of about  $576 \mu\text{m} \times 576 \mu\text{m}$  were obtained with a  $20\times$   
272 objective lens.

## 273 **4. Result and Discussion**

### 274 **4.1. Mechanical behaviour of core-shell microparticles**

275 Our next objective is investigating the mechanical strength of core-shell particles with liquid  
276 core under compression. Figure 5 compares the force-displacement relationships of the model  
277 and the experiment. The models can predict the deformation behaviour of the particle during  
278 compression as well as the maximum load a core-shell particle can bear. The force  
279 corresponding to a given displacement can be estimated using equation (2). Three sets of data  
280 from three core-shell geometries were prepared and investigated. As the core and the shell may  
281 not be centred (Fig. 6), the shell thickness is simply determined as the difference between the  
282 outer radius and the inner radius  $h=b-a$ , Fig. 2(b). The ratios of the shell thickness to outer  
283 radius  $h/b$  were 0.41, 0.33, and 0.21, Figure 6.

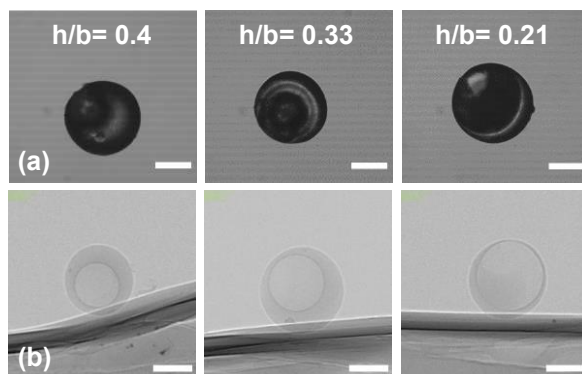


284

285 **Figure 5.** Force versus displacement characteristics of core-shell particles with different shell  
 286 thickness to outer radius ratios  $h/b$  of 0.41, 0.33, and 0.21.

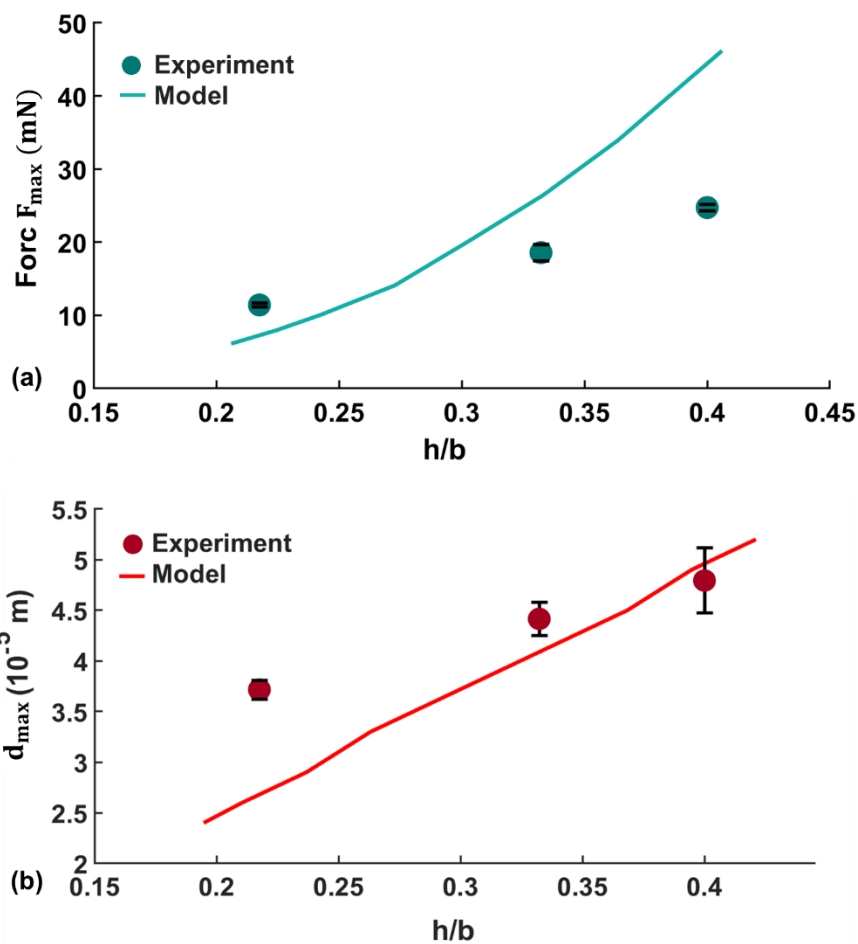
287 Figure 5 shows the force-displacement characteristics of these three particle geometries till  
 288 rupture. The data were fitted into equation (2) with  $A= 0.022$  and  $B= 0.034$  and show an  
 289 excellent agreement across all three geometries. The slight deviation of experimental data from  
 290 the theoretical curve might be caused by asymmetry of the core liquid in the shell, as observed  
 291 with X-ray images, Figure 6(b). The average asymmetry is about 25% in the x-y plane. Once  
 292 the top plate touched the particle and compressed it, the force started to increase until reaching  
 293 the critical displacement of rupture. The liquid contained in the shell causes it to bulge outwards  
 294 and prevent the shell to buckle at the critical displacement. Subsequently, at a displacement  
 295 beyond the critical rupture value, the liquid escapes and the force sharply dropped. Eventually,  
 296 as the shell gets entirely compressed and the plate hits the weighing pan surface, the force again  
 297 began to sharply increase. The critical displacement of rupture  $x_{\max}$  was estimated from  
 298 equation (3) by solving  $U_1 = U_2$  with  $C= -0.001$ . The corresponding rupture force of the critical  
 299 displacement  $d_{\max}$  can then be derived from equation (2). Figure 7(a) depicted the theoretical  
 300 and experimental rupture force for  $h/b$  ratios of 0.41, 0.33, and 0.21. The rupture force increases  
 301 with increasing ratio  $h/b$ . The results indicate that the rupture forces of the core-shell particles  
 302 with  $h/b$  ratios of 0.33 and 0.41 are almost 1.63 and 2.16 times greater than of the thins shell

303 with  $h/b=0.21$ . Figure 7(b) shows the relationship between the critical displacement  $d_{\max}$  and  
 304 the ratio  $h/b$ . The critical rupture displacement increases with increasing ratio  $h/b$ .



305  
 306 **Figure 6.** Images of core-shell microparticles used in the experiments: (a) Light microscopy;  
 307 (b) X-ray computed microtomography. The shell thickness to outer radius ratios are 0.4, 0.33,  
 308 and 0.21. Scale bars represent 100  $\mu\text{m}$ .

309



310

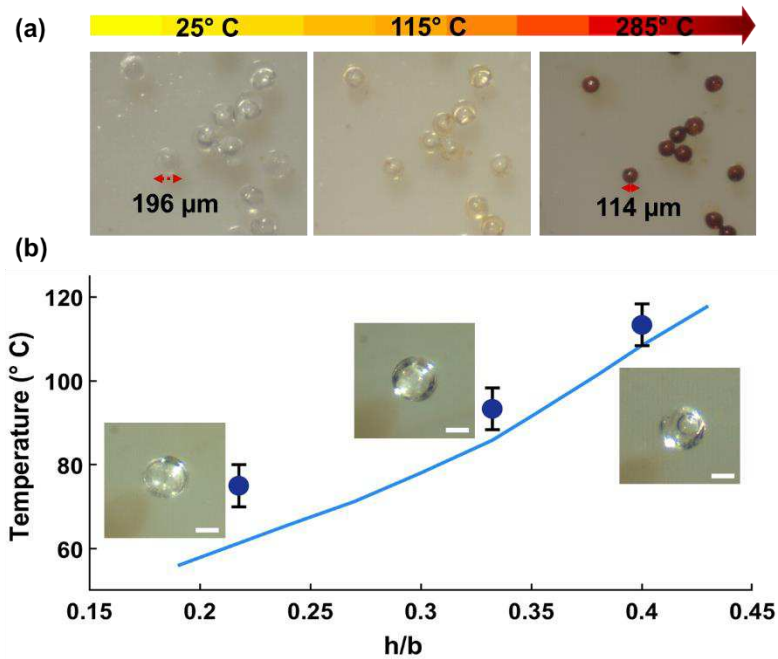
311 **Figure 7.** Critical rupture point as function of  $h/b$  ratio: (a) Rupture force; (b) The critical  
312 displacement  $d_{\max}$ .

313

#### 314 **4.2. Thermal behaviour of core-shell microparticles**

315 We first investigated the thermal behaviour of the core-shell microparticles  
316 experimentally by increasing the temperature and monitoring their response. Figure 8 shows  
317 representative core-shell microparticles with an outer diameter of approximately 196  $\mu\text{m}$  and a  
318 shell thickness of approximately 40  $\mu\text{m}$ . The ratio between the thickness and the outer diameter  
319 is therefore approximately  $h/b=0.41$ . Figure 8 indicates no significant changes in the particles  
320 until the temperature reached 115°C. The results imply that the core-shell particles maintain  
321 their shape and are stable up to this critical temperature. The polymeric shell encapsulating the  
322 oil core remained intact, without any leakage before reaching this temperature. According to  
323 Figure 8, the core-shell particles began to fracture and shrink after 115° C. The gradual  
324 perforation of solid shell could be due to the expansion of the oil core encapsulated inside the  
325 particle upon heating. The expansion of the oil core causes the internal pressure to rise until it  
326 exceeds the tensile strength of the shell layer.<sup>[17]</sup> After prolonged heating at temperature higher  
327 than the critical value, the core-shell particles appear to be hollow. Continuing to elevate the  
328 temperature causes the shell to turn brown and shrink. Figure 8 indicates that the core-shell  
329 particles were visibly destroyed at the temperature of 285° C. We also repeated this experiment  
330 for core-shell particles with ratios of  $h/b=0.21$  and  $h/b=0.33$  to determine their critical rupture  
331 temperature. We utilised the rupture force values obtained from the compression test to estimate  
332 the critical temperatures of the core-shell particles during the heating process. The  
333 corresponding critical rupture temperatures could be obtained from Equation (9). Using the  
334 measured critical forces of Fig. 8(b), the critical rupture temperatures estimated with (10) for  
335 particles with  $h/b$  ratios of 0.21, 0.33, and 0.41 are 62°C, 86°C, and 109°C, respectively. The  
336 experimental critical temperatures of the same set of  $h/b$  ratios are  $75\pm 5^\circ\text{C}$ ,  $95\pm 5^\circ\text{C}$  and

337  $115 \pm 5^\circ\text{C}$  and agree reasonably well with the analytical model. Figure 8(b) indicates that the  
 338 critical temperature increases with increasing  $h/b$  ratios or increasing shell thickness.



339  
 340 **Figure 8.** (a) Core-shell particles subjected to heating at elevated temperatures ranging from  
 341  $25^\circ\text{C}$  to  $285^\circ\text{C}$ ; (b) Critical rupture temperature as function of  $h/b$  ratio.

342 The above behaviour can be explained with the model of a thick-walled spherical shell  
 343 filled with a liquid that induced a uniform pressure due to thermal expansion. The volume  
 344 expansion coefficient  $\alpha = 1.29 \times 10^{-3} \text{ K}^{-1}$  is assumed to remain constant. According to equation  
 345 (9), there is a linear relationship between the pressure on inner wall of the shell and the  
 346 temperature. The pressure difference to the ambient leads to a radial normal stress. The induced  
 347 stress on the shell can be estimated using equation (11). For simplicity, the radial normal stress  
 348  $\sigma_r$  is considered zero on the outer surfaces. The maximum stress is at the inner surface at  $r=a$ ,  
 349 Fig. 2(b):

$$350 \sigma_{r,\max} = -P_{i2}. \quad (12)$$

351 The critical maximum stress depends on the internal pressure proportional to the  
 352 temperature of liquid core in the deformed state and the material properties of the core. The

353 maximum stress our microparticles could endure is approximately  $\sigma_{r,\max} = 1.46$  MPa as  
354 estimated from equation (12).

## 355 **5. Conclusion**

356 We studied liquid core-shell particles subjected to thermal and compression loads. We  
357 established analytical models for the thermal and mechanical behaviour of thick-walled liquid  
358 core-shell particle under heating and compression. We found that the maximum internal  
359 pressure induced by the heated liquid core depends on the volume expansion coefficient and  
360 isothermal compressibility of the liquid. We note that a relatively thick shell made of TMPTMA  
361 and a thickness to ratio  $h/b=0.41$  has a considerable thermal stability and can tolerate the  
362 thermal expansion of HFE7500 oil core up to 115° C. In addition, we characterised the  
363 mechanical behaviour of this thick wall core-shell particles. The compression of the core-shell  
364 particle between two horizontal plates and the critical rupture force were modelled analytically.  
365 We conducted validation experiments with three different particle geometries. The force-  
366 displacement characteristics predicted by the analytical model agreed well with experimental  
367 data across all three particle geometries. Our findings suggest that the rupture behaviour of  
368 core-shell particles under compression depends on the ratio between the shell thickness and the  
369 outer radius. The rupture force increases with increasing thickness to radius ratio. In conclusion,  
370 the TMPTMA-based core-shell particles with a liquid core demonstrated good mechanical and  
371 thermal behaviour. These microparticles promise potential applications as capsule for storage  
372 and micro reaction.

## 373 **Conflicts of interest**

374 There are no conflicts of interest to declare.

## 375 **Acknowledgement**

376 The microfluidic device was fabricated in Queensland Microtechnology Facility, part of the  
377 Queensland node-Griffith of the Australian National Fabrication Facility, a company  
378 established under the National Collaborative Research Infrastructure Strategy to provide nano  
379 and microfabrication facilities for Australia's researchers. N. T. Nguyen acknowledges support  
380 from the Australian Research Council grant DP180100055.

## 381 **References**

- 382 [1] Galogahi, F.M., Y. Zhu, H.J. An, and N.T. Nguyen, Core-shell microparticles:  
383 Generation approaches and applications, *Journal of Science-Advanced Materials and*  
384 *Devices*. 5 (2020) 417-435. <https://doi.org/10.1016/j.jsamd.2020.09.001>.
- 385 [2] Yow, H.N. and A.F. Routh, Formation of liquid core–polymer shell microcapsules, *Soft*  
386 *Matter*. 2 (2006) 940-949. <https://doi.org/10.1039/b606965g>.
- 387 [3] Li, Q., X. Liu, X. Wang, S. Qiu, K. Byambasuren, L. Dang, and Z. Wang,  
388 Antiproliferative ability and fluorescence tracking of  $\alpha$ -linolenic acid-loaded  
389 microemulsion as label-free delivery carriers in MDA-MB-231 cells, *Journal of*  
390 *agricultural and food chemistry*. 67 (2019) 11518-11526.  
391 <https://doi.org/10.1021/acs.jafc.9b04972>.
- 392 [4] Tiribocchi, A., A. Montessori, M. Lauricella, F. Bonaccorso, S. Succi, S. Aime, M.  
393 Milani, and D.A. Weitz, The vortex-driven dynamics of droplets within droplets, *Nature*  
394 *Communications*. 12 (2021) 1-10. <https://doi.org/ARTN 82>  
395 [10.1038/s41467-020-20364-0](https://doi.org/10.1038/s41467-020-20364-0).
- 396 [5] Wang, H., Z. Zhao, Y. Liu, C. Shao, F. Bian, and Y. Zhao, Biomimetic enzyme cascade  
397 reaction system in microfluidic electrospray microcapsules, *Sci Adv*. 4 (2018) eaat2816.  
398 <https://doi.org/10.1126/sciadv.aat2816>.

- 399 [6] Nguyen, N.T., S. Schubert, S. Richter, and W. Dotzel, Hybrid-assembled micro dosing  
400 system using silicon-based micropump/valve and mass flow sensor, *Sensors and*  
401 *Actuators a-Physical*. 69 (1998) 85-91. <https://doi.org/Doi> 10.1016/S0924-  
402 4247(98)00039-9.
- 403 [7] Dinh, T., H.P. Phan, A. Qamar, P. Woodfield, N.T. Nguyen, and D.V. Dao,  
404 Thermoresistive Effect for Advanced Thermal Sensors: Fundamentals, Design  
405 Considerations, and Applications, *Journal of Microelectromechanical Systems*. 26  
406 (2017) 966-986. <https://doi.org/10.1109/Jmems.2017.2710354>.
- 407 [8] Dinh, T., H.P. Phan, D.V. Dao, P. Woodfield, A. Qamara, and N.T. Nguyen, Graphite  
408 on paper as material for sensitive thermoresistive sensors, *Journal of Materials*  
409 *Chemistry C*. 3 (2015) 8776-8779. <https://doi.org/10.1039/c5tc01650a>.
- 410 [9] Bandara, T., N.T. Nguyen, and G. Rosengarten, Slug flow heat transfer without phase  
411 change in microchannels: A review, *Chemical Engineering Science*. 126 (2015) 283-  
412 295. <https://doi.org/10.1016/j.ces.2014.12.007>.
- 413 [10] Mytnyk, S., I. Ziemecka, A.G.L. Olive, J.W.M. van der Meer, K.A. Totlani, S.  
414 Oldenhof, M.T. Kreutzer, V. van Steijn, and J.H. van Esch, Microcapsules with a  
415 permeable hydrogel shell and an aqueous core continuously produced in a 3D  
416 microdevice by all-aqueous microfluidics, *Rsc Advances*. 7 (2017) 11331-11337.  
417 <https://doi.org/10.1039/c7ra00452d>.
- 418 [11] Shchukin, D.G., G.B. Sukhorukov, and H. Möhwald, Smart inorganic/organic  
419 nanocomposite hollow microcapsules, *Angewandte Chemie International Edition*. 42  
420 (2003) 4472-4475. <https://doi.org/10.1002/anie.200352068>.
- 421 [12] Mercadé-Prieto, R., R. Allen, Z. Zhang, D. York, J.A. Preece, and T.E. Goodwin,  
422 Failure of elastic-plastic core-shell microcapsules under compression, *AIChE journal*.  
423 58 (2012) 2674-2681. <https://doi.org/10.1002/aic.12804>.

- 424 [13] Fujiwara, M., K. Shiokawa, K. Morigaki, Y.C. Zhu, and Y. Nakahara, Calcium  
425 carbonate microcapsules encapsulating biomacromolecules, *Chemical Engineering*  
426 *Journal*. 137 (2008) 14-22. <https://doi.org/10.1016/j.cej.2007.09.010>.
- 427 [14] Caruso, M.M., B.J. Blaiszik, H. Jin, S.R. Schelkopf, D.S. Stradley, N.R. Sottos, S.R.  
428 White, and J.S. Moore, Robust, double-walled microcapsules for self-healing polymeric  
429 materials, *ACS Appl Mater Interfaces*. 2 (2010) 1195-9.  
430 <https://doi.org/10.1021/am100084k>.
- 431 [15] Kang, S., M. Baginska, S.R. White, and N.R. Sottos, Core-shell polymeric  
432 microcapsules with superior thermal and solvent stability, *ACS Appl Mater Interfaces*.  
433 7 (2015) 10952-6. <https://doi.org/10.1021/acsami.5b02169>.
- 434 [16] Fung, W.T., A. Beyzavi, P. Abgrall, N.T. Nguyen, and H.Y. Li, Microfluidic platform  
435 for controlling the differentiation of embryoid bodies, *Lab Chip*. 9 (2009) 2591-5.  
436 <https://doi.org/10.1039/b903753e>.
- 437 [17] Vasudevan, D., R.R. Gaddam, A. Trinchì, and I. Cole, Core-shell quantum dots:  
438 Properties and applications, *Journal of Alloys and Compounds*. 636 (2015) 395-404.  
439 <https://doi.org/10.1016/j.jallcom.2015.02.102>.
- 440 [18] Liu, S., S.N. Reed, M.J. Higgins, M.S. Titus, and R. Kramer-Bottiglio, Oxide rupture-  
441 induced conductivity in liquid metal nanoparticles by laser and thermal sintering,  
442 *Nanoscale*. 11 (2019) 17615-17629. <https://doi.org/10.1039/c9nr03903a>.
- 443 [19] Latnikova, A. and A. Yildirim, Thermally induced release from polymeric  
444 microparticles with liquid core: the mechanism, *Soft matter*. 11 (2015) 2008-2017.  
445 <https://doi.org/10.1039/C4SM02674H>.
- 446 [20] Zhao, H., X. Fei, L. Cao, S. Zhao, and J. Zhou, Changes in microcapsules under heating:  
447 the effect of particle size on thermal stability and breakability, *Journal of Materials*  
448 *Science*. 55 (2020) 3902-3911. <https://doi.org/10.1007/s10853-019-04297-8>.

- 449 [21] Leopércio, B.C., M. Michelon, and M.S. Carvalho, Deformation and rupture of  
450 microcapsules flowing through constricted capillary, *Scientific Reports*. 11 (2021) 1-  
451 12. <https://doi.org/10.1038/s41598-021-86833-8>.
- 452 [22] Perez, R.A. and H.W. Kim, Core-shell designed scaffolds for drug delivery and tissue  
453 engineering, *Acta Biomater.* 21 (2015) 2-19.  
454 <https://doi.org/10.1016/j.actbio.2015.03.013>.
- 455 [23] Neubauer, M.P., M. Poehlmann, and A. Fery, Microcapsule mechanics: from stability  
456 to function, *Adv Colloid Interface Sci.* 207 (2014) 65-80.  
457 <https://doi.org/10.1016/j.cis.2013.11.016>.
- 458 [24] Zhang, G.S., Z. Mechanical properties of melamine-formaldehyde microcapsules,  
459 *Journal of microencapsulation*. 18 (2001) 593-602. [https://doi.org/](https://doi.org/10.1080/02652040010019541)  
460 [10.1080/02652040010019541](https://doi.org/10.1080/02652040010019541).
- 461 [25] Sun, G. and Z. Zhang, Mechanical strength of microcapsules made of different wall  
462 materials, *International Journal of Pharmaceutics*. 242 (2002) 307-311.  
463 [https://doi.org/Pii S0378-5173\(02\)00193-X](https://doi.org/Pii%20S0378-5173(02)00193-X)
- 464 Doi [10.1016/S0378-5173\(02\)00193-X](https://doi.org/10.1016/S0378-5173(02)00193-X).
- 465 [26] Risso, F. and M. Carin, Compression of a capsule: mechanical laws of membranes with  
466 negligible bending stiffness, *Phys Rev E Stat Nonlin Soft Matter Phys.* 69 (2004)  
467 061601. <https://doi.org/10.1103/PhysRevE.69.061601>.
- 468 [27] Liu, K.K., D.R. Williams, and B.J. Briscoe, Compressive deformation of a single  
469 microcapsule, *Phys Rev E Stat Phys Plasmas Fluids Relat Interdiscip Topics*. 54 (1996)  
470 6673-6680. <https://doi.org/10.1103/physreve.54.6673>.
- 471 [28] Carin, M., D. Barthes-Biesel, F. Edwards-Levy, C. Postel, and D.C. Andrei,  
472 Compression of biocompatible liquid-filled HSA-alginate capsules: determination of

- 473 the membrane mechanical properties, *Biotechnol Bioeng.* 82 (2003) 207-12.  
474 <https://doi.org/10.1002/bit.10559>.
- 475 [29] Ansari, A. and M. Abbaspour, Modelling and economic evaluation of pressure-retarded  
476 osmosis power plant case study: Iran, *International Journal of Ambient Energy.* 40  
477 (2019) 69-81. <https://doi.org/10.1080/01430750.2017.1354323>.
- 478 [30] Bando, K., K. Ohba, and Y. Oiso, Deformation analysis of microcapsules compressed  
479 by two rigid parallel plates, *Journal of biorheology.* 27 (2013) 18-25.  
480 <https://doi.org/10.1007/s12573-012-0053-8>.
- 481 [31] Taber, L.A., Large Deflection of a Fluid-Filled Spherical-Shell under a Point Load,  
482 *Journal of Applied Mechanics-Transactions of the Asme.* 49 (1982) 121-128.  
483 <https://doi.org/Doi 10.1115/1.3161953>.
- 484 [32] Rachik, M., D. Barthes-Biesel, M. Carin, and F. Edwards-Levy, Identification of the  
485 elastic properties of an artificial capsule membrane with the compression test: effect of  
486 thickness, *J Colloid Interface Sci.* 301 (2006) 217-26.  
487 <https://doi.org/10.1016/j.jcis.2006.04.062>.
- 488 [33] Teo, A.J.T., F. Malekpour-Galogahi, K.R. Sreejith, T. Takei, and N.T. Nguyen,  
489 Surfactant-free, UV-curable core-shell microcapsules in a hydrophilic PDMS  
490 microfluidic device, *Aip Advances.* 10 (2020) 065101.  
491 <https://doi.org/10.1063/5.0004736>.
- 492 [34] Galogahi, F.M., Y. Zhu, H. An, and N.-T. Nguyen, Formation of core-shell droplets for  
493 the encapsulation of liquid contents, *Microfluidics and Nanofluidics.* 25 (2021) 1-11.  
494 <https://doi.org/10.1007/s10404-021-02483-2>.
- 495 [35] Pauchard, L. and S. Rica, Contact and compression of elastic spherical shells: the  
496 physics of a ‘ping-pong’ball, *Philosophical Magazine B.* 78 (1998) 225-233.  
497 <https://doi.org/10.1080/13642819808202945>.

- 498 [36] Shorter, R., J. Smith, V. Coveney, and J. Busfield, Axial compression of hollow elastic  
499 spheres, *Journal of Mechanics of Materials and Structures*. 5 (2010) 693-705.  
500 <https://doi.org/10.2140/jomms.2010.5.693>.
- 501 [37] Young, W.C., R.G. Budynas, and A.M. Sadegh, *Roark's formulas for stress and strain*,  
502 ed., McGraw-Hill Education, 2012.
- 503 [38] Borgnakke, C. and R.E. Sonntag, *Fundamentals of thermodynamics*, ed., John Wiley &  
504 Sons, 2020.
- 505 [39] Fang, D., Y. Li, X. Meng, and J. Wu, Liquid density of HFE-7200 and HFE-7500 from  
506 T=(283 to 363) K at pressures up to 100 MPa, *The Journal of Chemical*  
507 *Thermodynamics*. 69 (2014) 36-42. <https://doi.org/10.1016/j.jct.2013.09.035>.
- 508 [40] Sreejith, K.R., L. Gorgannezhad, J. Jin, C.H. Ooi, T. Takei, G. Hayase, H. Stratton, K.  
509 Lamb, M. Shiddiky, D.V. Dao, and N.T. Nguyen, Core-Shell Beads Made by Composite  
510 Liquid Marble Technology as A Versatile Microreactor for Polymerase Chain Reaction,  
511 *Micromachines (Basel)*. 11 (2020) 242. <https://doi.org/10.3390/mi11030242>.
- 512

## Supplementary Files

This is a list of supplementary files associated with this preprint. Click to download.

- [SupportingInformation1.docx](#)